J. Earth Syst. Sci. (2020)129 76
https://doi.org/10.1007/s12040-019-1334-z

Episodic ferricretization of the Deccan Laterites (India): Inferences from ore microscopy, mineral magnetic and XRD spectroscopic studies

Jyotibala Singh[1], S J Sangode[1,*], M F Bagwan[1], D C Meshram[1] and Anup Dhobale[2]

[1]*Department of Geology, Savitribai Phule Pune University, Pune, India.*
[2]*Department of Geology, R. T. M. Nagpur University, Nagpur, India.*
**Corresponding author. e-mail: sangode@rediffmail.com*

MS received 27 June 2019; revised 2 October 2019; accepted 1 November 2019

Studies based on sampling a ∼40 m thick profile comprising the basalt protolith, saprolitic horizon and various levels of ferricretization in the Deccan upland lateritic sequence of the western Maharashtra (India), indicated episodic nature of lateritization. Mineral magnetism precisely demarcated the ferrimagnetic to anti-ferromagnetic (fm/afm) boundary at the base followed by various stages of lateritic developments in the upper horizons. The fm/afm boundary can be traced in field using magnetic susceptibility and therefore provide a datum for laterite base-level mapping. Ore microscopy details the inter-association and paragenesis of amorphous and crystalline varieties of iron oxide minerals (hematite, limonite, goethite) that are further modified by allochthonous inputs and changes in porosity. The lowermost horizons show silcretization, while the XRD studies record sporadic kaolinitic occurrence throughout the profile with gibbsite appearing in the upper part of the profile. Combination of mineral magnetic and ore microscopic observations depict frequent lateral inputs possibly during periods of heavy precipitation arresting and further reclaiming the process of lateritization to produce large composite thicknesses of the Deccan lateritic sequence without matured lateritization.

Keywords. Ferricrete; Deccan high level laterites; mineral magnetism; ore microscopy; XRD; India.

1. Introduction

Cenozoic laterites in India are mostly studied from the Deccan West coast referred to as deeply weathered paleo-surfaces (Schmidt *et al.* 1983; Kumar 1986; Patel 1987; Ollier and Rajaguru 1989; Sahasrabudhe and Rajaguru 1990; Achyuthan 1996; Widdowson 1997; Widdowson and Gunnell 1999; Borger and Widdowson 2001; Ollier and Sheth 2008; Bonnet *et al.* 2014, 2016). These laterites are further classified into (1) 'high-level laterites' capping the summits of hill and plateau, and (2) 'low-level laterites' occurring at coastal low lands (Widdowson and Cox 1996). Present study focuses on the high-level-laterites for which we prefer to use the term 'Deccan Upland Laterites' (DUL) for the laterites occurring over >1000 m approximate altitudes) compared to the low-level laterites (<300 m) near the coast. Conflicting theories do exist on the origin and evolution of DUL describing it as primary (/autochthonous) or of allochthonous nature (see, Widdowson and Cox 1996; Widdowson 1997; Widdowson and Gunnell 1999; Borger and Widdowson 2001; Wimpenny

Published online: 20 February 2020

et al. 2007; Mishra *et al.* 2007; Widdowson 2007; Ollier and Sheth 2008; Babechuk *et al.* 2014, 2015). Large thicknesses of laterites (ferricrete + saprolite >20 m) are observed in the DUL without clear gradation or horizonation of weathering fronts compelling the use of terms ferricrete and lateritic profiles by the above authors. All these aspects demand more detailed studies on their mineralogical evolution particularly by understanding the mobilization, re-mobilization and precipitation of iron and Al oxides and hydroxides. We attempt an integrated approach of mineral magnetism, spectroscopy and ore microscopy to study one of the ideal profiles within the DUL sequence.

Amongst the Indian lateritic occurrences, Deccan laterites uniquely represent a ferrimagnetically rich protolith. This favours an ideal application of mineral magnetism which allows several semi-quantitative estimates on ferri- and anti-ferromagnetic mineral concentrations within their mixtures (see, Thompson and Oldfield 1986; Heller and Evans 1995; Jordanova and Petersen 1999; Balsam *et al.* 2004; Sangode and Bloemendal 2004; Torrent *et al.* 2006; Liu *et al.* 2006, 2007, 2012; Long *et al.* 2011, 2015; Buggle *et al.* 2014; Srivastava *et al.* 2015). Forms of iron oxides are the imprints of style of its mobilizations, dissolution, precipitation and transformations as a result of the ongoing process of lateritization/ferricretization (Amouric *et al.* 1986; Anand and Gilkes 1987; Beauvais and Colin 1993; Schellmann 1994; Zeese *et al.* 1994; Cornell and Schwertmann 2003; Meshram and Randive 2011). Further, the iron oxides once transformed and precipitated from solution, tend to remain stable through a large number of overriding geological and geochemical changes (Schwertmann 1958, 1988, 1993; Turner 1997; Schwertmann and Cornell 2000). The well-established mineral magnetic approach provides data based approximation on the above processes, based on qualitative and semi-quantitative changes within the iron oxide compounds (Thompson and Oldfield 1986; Heller and Evans 1995; Jordanova and Petersen 1999; Balsam *et al.* 2004; Sangode and Bloemendal 2004; Torrent *et al.* 2006; Liu *et al.* 2006, 2007, 2012; Long *et al.* 2011, 2015; Buggle *et al.* 2014; Srivastava *et al.* 2015).

In field and under microscope, iron oxides are expressed by their distinct colours and mottling characteristics (Torrent *et al.* 1980; Turner 1997; Schwertmann and Cornell 2000), and therefore ore microscopy is one of the most fundamental approach to be integrated with mineral magnetism. The spectroscopic methods like XRD further help to identify the clay minerals reflecting the distribution of aluminum oxides/hydroxides. Present approach therefore integrates these different methods to analyze a well exposed section of lateritic profile in DUL.

2. Study area

The Western Ghat Escarpment (WGE) parallels the West Coast of India which has provided conducive-tropical humid conditions for development of laterites during entire Cenozoic time. The WGE covers northern Deccan basalt and the southern non-basaltic (Archean–Proterozoic) terrain with reference to the nature of protolith (Widdowsow and Gunnell 2009). The study area falls in Patan in Satara district of southern Maharashtra (figure 1) near latitude of 17°68′05″N. The large plateau of Patan near Satara district of Maharashtra ideally represents part of the upland lateritic occurrence in the West Coast of India. Previously Widdowson (1997) and Ollier and Sheth (2008) studied the DUL and such duricrusts from the Bamnoli Range in the Satara–Patan–Koyna region.

Patan litho-section (PLL) selected for the present attempt falls in Bamnoli range and represent ∼42 m thick well exposed road cutting (figures 2 and 3). This profile encompasses unaltered basalt, weathered basalt, saprolitic horizon and variants of lateritic/ferricrete horizons up to the top. The detailed field megascopic characters and lithology of the PLL profile is documented and summarized in table 1 and figure 4.

3. Methodology

Block sampling was conducted by observing gradual changes within the profile (e.g., see figures 2 and 3). Since the studies were aimed at finding the changes in vertical profile, the units are denoted based on observations of meter-scale variations described in table 1 and figure 4. This allowed us to collect the samples showing visual changes in the nature of iron oxide zones maintaining a relatively close sampling interval. The field description is integrated with morphological observations of hand specimen and the ore microscopic observations described in the text later. About 2–3 kg of intact hand samples representing each unit was

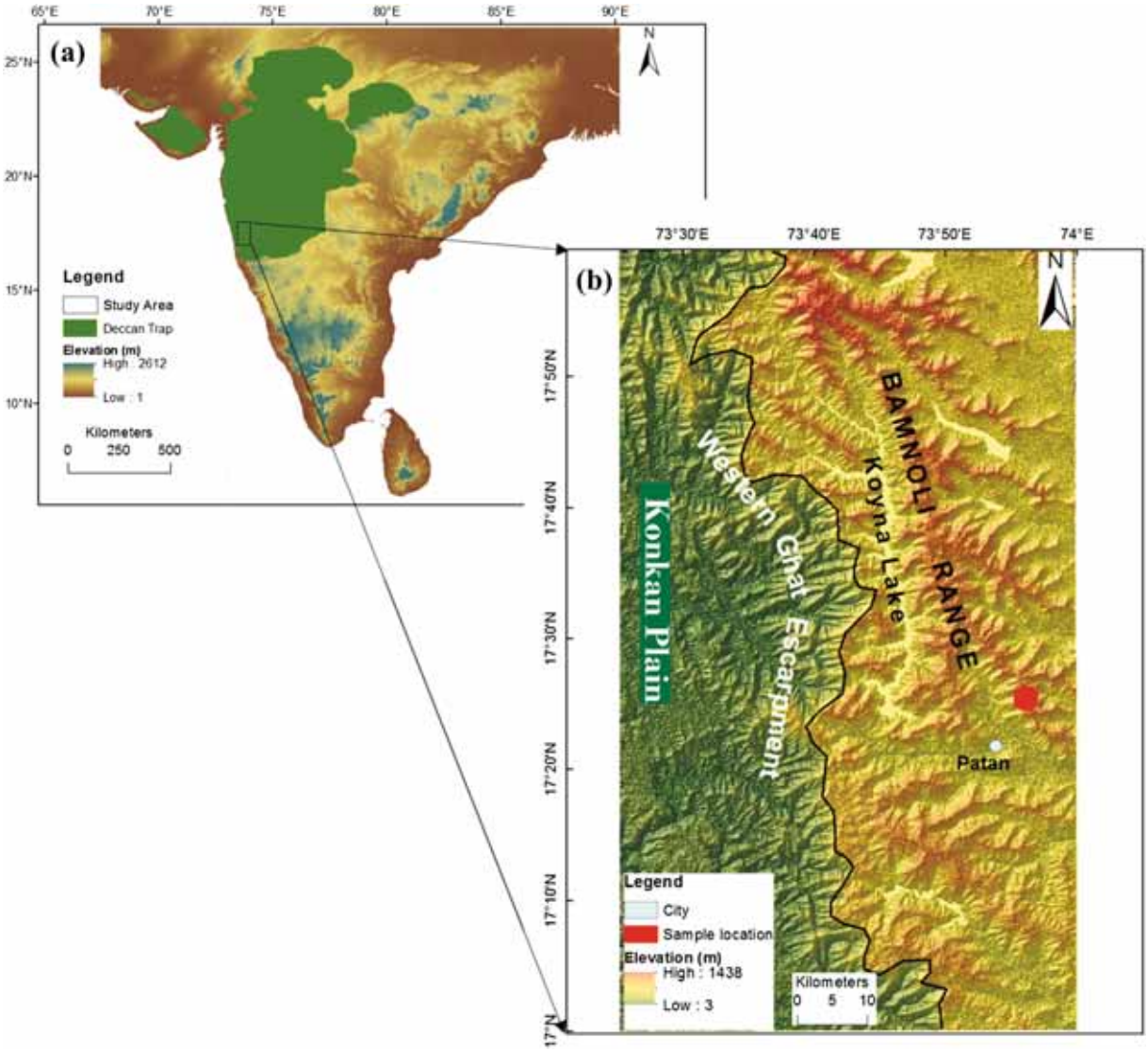

Figure 1. (**a**) SRTM image of southern part of Indian subcontinent showing the extent of Deccan traps and (**b**) digital elevation model of Western Ghats showing Bamnoli range where the studied location of Patan area is shown by red filled circle.

taken for the 23 units (table 1). For mineral magnetic, ore microscopic and XRD studies, representative chunks were selected and some special samples were collected as limonitic, hematitic and brownish grey rich pockets. For ore microscopy dry samples of $\sim$2.5 cm^2 were dipped into resin and soaked overnight in vacuum impregnation unit. The polished thin sections were prepared using Beuhler preparation units and observed under reflecting microscope (at 5×, 10×, and 20× magnifications). For rock magnetism, representative fragments of the sample were filled and tightly packed using cling film into standard polystyrene bottles supplied by Bartington, UK. For XRD, about 50 gm of samples from each unit was powdered and thoroughly mixed to have bulk mineralogical representation.

3.1 *Rock magnetism*

The magnetic susceptibility (χ_{lf}) was measured using Bartington MS 2B laboratory sensor at duel frequency modes (0.46 and 4.6 kHz). The susceptibilities were subjected to air- and empty pot corrections before mass normalization. The frequency dependent susceptibility (χ_{fd}) and its percentage (χ_{fd}%) were calculated as: $\chi_{lf} - \chi_{hf}$ and $[(\chi_{lf} - \chi_{hf})/\chi_{lf}] \times 100$, respectively. The χ_{lf} is very sensitive to ferrimagnetic concentration producing higher values while the anti-ferromagnetic composition produces relatively lower values even at higher concentration. The χ_{fd} discriminates the small fraction of finer ferromagnetic grains (often pedogeneic) in general and may represent pigmentary or other finer forms in case of anti-ferromagnetism.

Figure 2. Field photographs of the Patan lateritic (PLL) section; (**a**) panoramic view of the Patan plateau top; (**b**) Saprolitic zone encountered in the lowermost part of the profile; (**c**) succeeding lateritic zones; and (**d**) the topmost surface of the studied profile showing limonitic growth.

The anhysteretic remanence magnetization (ARM) was grown at 200 mT peak field superimposed over 0.1 mT DC bias fields using Magnon alternating field demagnetizer. The mass normalized ARM was further normalized with DC field to represent susceptibility of anhysteretic remanance (χ_{ARM}). The χ_{ARM} enables discrimination of the stable single domain (SD) grains within ferri/anti-ferromagnetic assemblages. The SD grains are often authigenic ferrimagnets grown under less oxidative to reducing conditions. However, the expression of χ_{ARM} under highly anti-ferromagnetic context of laterites is not established. Isothermal remanence magnetization (IRM) was induced using impulse magnetizer (ASC-IM-10-30, US), and measured using minispin fluxgate spinner magnetometer. The meaning of IRM spectra is similar to the hysteresis loop but it is more convenient to use the IRM data to develop suitable parameters and ratios especially in unique mineralogies like that of laterites. A maximum available field of 2500 mT was used to find the mass normalized value of Saturation Isothermal Remanent Magnetization (SIRM). The parameter Hard Isothermal Remanent Magnetization (HIRM) was estimated as HIRM = 0.5 × (SIRM + IRM_{-300} mT); where IRM_{-300} mT is the back-field remanance at 300 mT. The Soft-IRM was calculated as $Soft_{IRM}$ = 0.5 × (SIRM − IRM_{-20} mT), where IRM_{-20} is the back-field remanance at 20 mT. The parameter coercivity of remanent [$B_{(0)CR}$] is estimated as the reverse DC field required to reduce the SIRM to zero. The S-ratio was calculated as IRM_{-300mT}/SIRM and IRM_{-100}/SIRM. A combination of all these parameters can produce information on relative changes in the ferri- to anti-ferromagnetic compositions and their mineralogical variation within the profile. The Deccan basalt comprising of significant ferrimagnetic mineralogy (magnetite-titanomagnetites), the process of lateritization is characteristic of the anti-ferromagnetic minerals (hematite, goethite and limonites). The above mineral magnetic parameters are most sensitive to such change in mineralogy and their concentration.

3.2 *X-ray diffraction studies*

The bulk powder samples (230 mesh) from each unit were analyzed using Rigaku XRD Model Ultima IV. The scans were run using Cu–Kα anode with a voltage of 45 KV and the intensity of 40 mA. The scan range used in the present case is 3 to 60°–2 θ with step interval of 0.0200^{θ} at the speed of 4.0 per second.

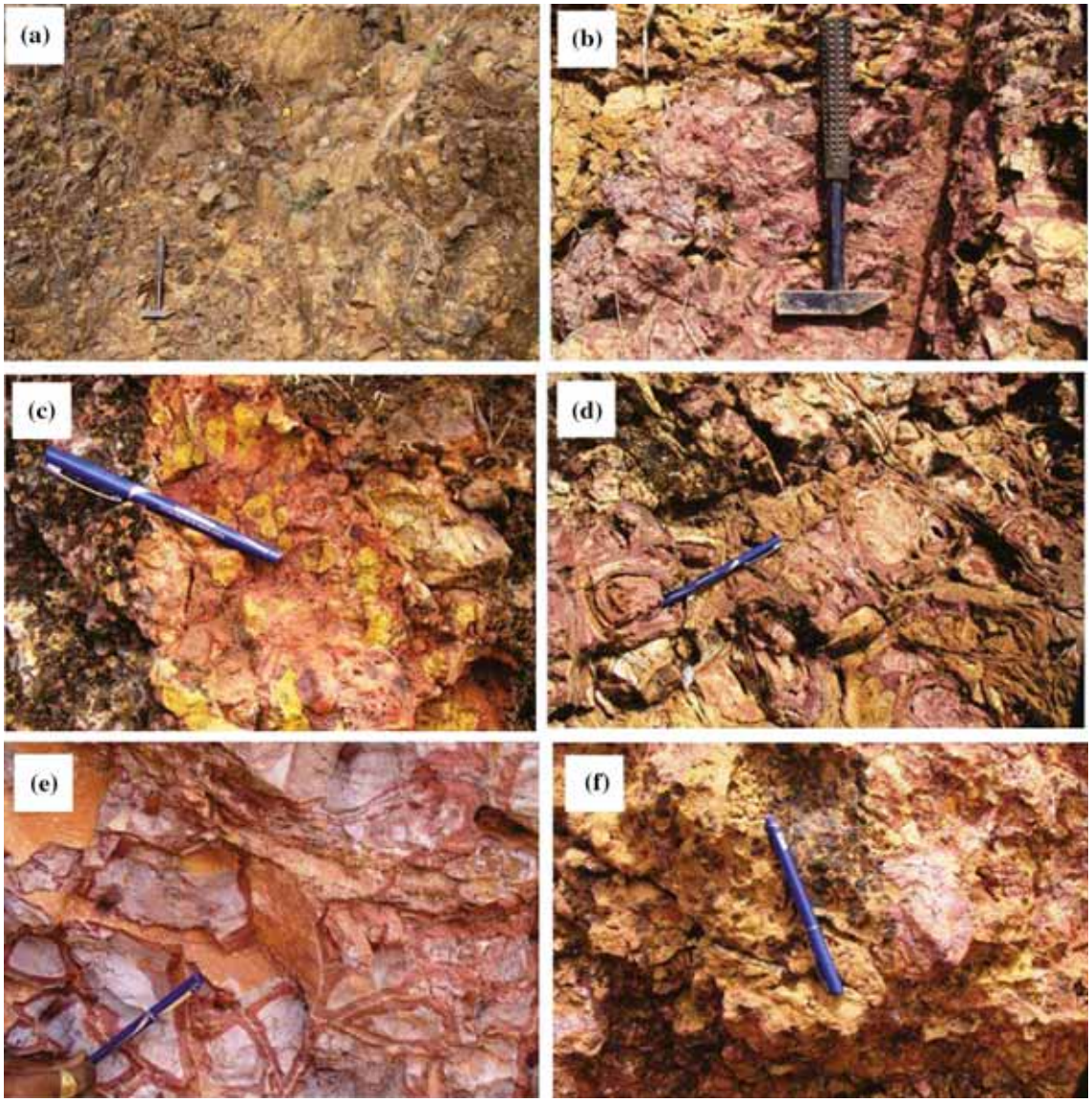

Figure 3. Close-up megascopic photographs of the selective features observed in the studied profile. (**a**) Incipient saprolitic zone; (**b**) weakly developed nodular spheroids; (**c**) interspersed hematite–limonite growth; (**d**) solution activity with nodular development; (**e**) mature stage with initial bauxitization; and (**f**) upper zone with higher porosity and higher limonite content.

4. Results and inferences

4.1 *Field-megascopic and ore microscopic observations*

A description from field megascopic observations (accounted in table 1), hand specimens (figure 4) and polished sections (figure 5) for each sampled horizon has been integrated and produced below.

The lowermost unit PLL-1 in hand specimen shows basaltic core surrounded by weathering rinds (figure 4). The polished section for the weathering rind shows coarse granular groundmass with micro-tubes filled by limonite (see figure 5a). Majority of the groundmass show yellowish-red coloured hematite–limonite transitions along with patches filled by limonite suggesting secondary filling of the pore spaces. The micro-tubes filled with limonite are common in the lower part suggesting incipient porosity and solution activity. Isolated, unweathered to partly weathered rock fragments (in millimeters scale) are also seen (figure 5a). However, the coercivity and S-ratios of this sample is too low to infer any antiferromagnetism, and the ferrimagnetic minerals still dominate the magnetic property depicting its affinity towards bed rock composition. This suggests possible amorphous/poorly crystalline pigmentary nature of the visible hematite being

Table 1. *Litholog for the Patan laterite (PLL) section representing sample collected along with nature of sampling horizons.*

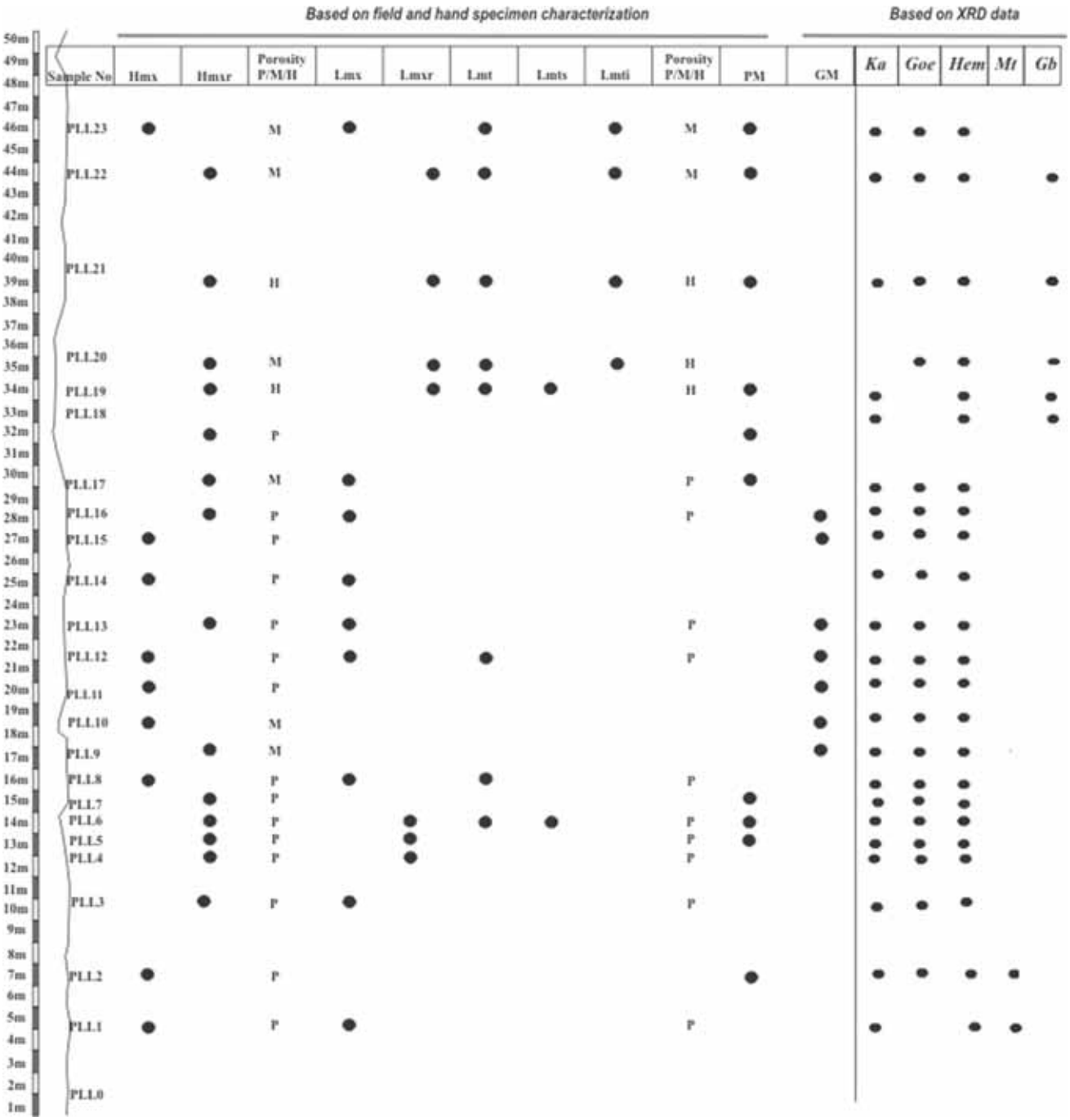

The details in each horizon are comparatively presented with abbreviations. Hmx: hematite matrix, Hmxr: hematite matrix with rock fragments, Porosity P/M/H (i.e., poor, medium and high), Lmx: limonitic matrix, Lmxr: limonitic matrix with rock fragments, Lmt: limonitic boundaries (i.e., diffuse boundaries), Lmts: limonitic matrix isolated, Lmti: limonitic sharp boundaries interlocked, PM: pink mottling, GM: grey mottling.

weakly responding to the magnetic properties in the mixture dominated by ferrimagnetic mineralogy of the basalt protolith.

The overlying horizon, PLL-2 shows dominant hematite (reddish) and massive groundmass. In hand specimen and microscopic scales the hematite appears as very fine grained, dull to pinkish red due to its amorphous nature as discussed above. Minor diffused limonitic (yellowish) mottling can be seen interspersed within the groundmass. Under microscope PLL-2 appears similar to PLL-1, but with more intense hematization with relatively

Figure 4. Megascopic photographs representing hand specimen and their variation along profile. The sampling strategy present the field notation where the partly weathered bedrock is numbered PLL-1.

larger irregular pore spaces filled by limonitic precipitation. This is marked as intense solution–precipitation activity in figure 5(b). The overlying horizon PLL-3 shows a change in colour to dull yellowish brown with incipient (diffused) development of nodules (marked by their bluish grey

colour). The hand specimen shows distinct brown and dull flesh coloured bands depicting precipitation of goethite and Al-hydroxides. Under microscope PLL-3 shows vermicular texture but with more intense weathering of plagioclase laths filled by limonite and silica. Further under higher resolution, the pores show distinct rounded boundaries filled with silica. The rock fragments are observed with decrease in size relative to that in PLL-1. The inter-associations indicate that the silcretization is followed by limonitization and hematization (figure 5c). The horizon PLL-4 shows compact brownish red coloured groundmass, dull yellowish brown matrix at places and poor porosity. Under microscope it shows vermicular texture dominated by dull yellow limonitic filling. The groundmass shows cherty filling with granular hematites and finely dispersed rock fragments (figure 5d). The sample PLL-5 is of similar nature to that of PLL-4. Under microscope it shows vermicular texture being replaced by granular and more porous texture marked by the pinkish red hematite. Scanty (patchy) limonitic filling is observed with remnant of weathered rock fragments in linear or clustered manner (see figure 5e). The horizon PLL-6 shows intermixed pink, yellow and yellowish brown massive hematite–limonite–cherty groundmass (figure 5f). It also shows some remnants of rock fragments suggesting influx of detrital/saprolite clasts. Under microscope, distinct limontic fillings are observed as against the white cherty filling of the pores in previous samples. The brown coloured filling probably indicate presence of goethite (see figure 5f). The sample PLL-7 shows prominent yellowish nodules within the background of pinkish red matrix. Diffused bluish grey vugs with remnant rock fragments are seen. In hand specimen, PLL-7 shows massive and somewhat intermixed complex of dull brownish red and light yellowish to brown coloured oxides. Under microscope this sample shows groundmass of dull yellow limonite to amorphous greyish brown iron oxide (goethite?). The hematite is almost negligible whereas dull amorphous brownish grey groundmass suggests goethite with limonitic mottling. The lath shaped filling of chert indicates replacement of plagioclase laths as common process (figure 5g). The sample PLL-8 under microscope shows saprolitic texture with some rock fragments and dominant hematite groundmass as well as silcretization and limonite precipitation (see figure 5h). Under microscope a major saprolitic rock fragment is noticed. More fragments of angular to subangular nature comprising of rock, saprolite and ferricrete with sharp to diffused boundaries further suggest incorporation of detrital influx subjected to lateritization. The previous horizons depicting goethitic groundmass indicate prevalent humid conditions that appears to have favoured such lateral detrital influxes observed in the unit PLL-8.

The sample PLL-9 shows massive hematization and limonite intermix activity with low porosity suggesting intense solution–precipitation activity. It also shows secondary filling by limonite, whereas megascopically this horizon showed notable change to light brown and grey colour with bluish grey diffused-large nodular development. The groundmass appears massive and flesh coloured with low porosity along with isolated and corroded rock fragments. This unit (PLL-10) appears contrastingly different by colour due to dark bluish grey nodular intergrowth in a dark reddish brown matrix. It shows hematite replacements within low porosity saprolitic groundmass. Under microscope it also shows saprolitic occurrence with weathered rock fragments bordered by hematite solution (figure 5j). This confirms the detrital influx of clasts from the exposed saprolitic upland that are further subjected to ferricretization. PLL-11 in hand specimen show incipient pisolitic development marked by bluish grey nodular textures and internal structure. Under thin section it shows massive hematitic–goethitic groundmass with scattered and isolated, highly weathered small rock fragments (figure 5k). PLL-12 shows hematite being replaced with limonite; and the lath shaped cherts depict replacement of feldspars (figure 5l). PLL-13 in hand specimen shows distinct bluish grey pisolites besides irregular yellowish (limonitic) masses within the hematitic groundmass. Under microscope it shows distinct saprolitic fragments with intense hematization and higher porosity and shows presence of white or bluish grey cherts (silcretes) (figure 5m). The colour of hematite is remarkably changed from pinkish red to bright cherry (brick) red depicting its change from amorphous to crystalline nature. Isolated patches (islands) of pinkish red hematite are seen and large weathered rock fragments are common. PLL-14 is an intermediate horizon with diffused bluish grey mottles under yellow to reddish brown groundmass. Under microscope it shows reddish hematite with transition from granular to dark brown and largely maroon coloured mixed groundmass; and the lath shaped silica filling (figure 5n). PLL-15 shows better development of limonitic matrix with

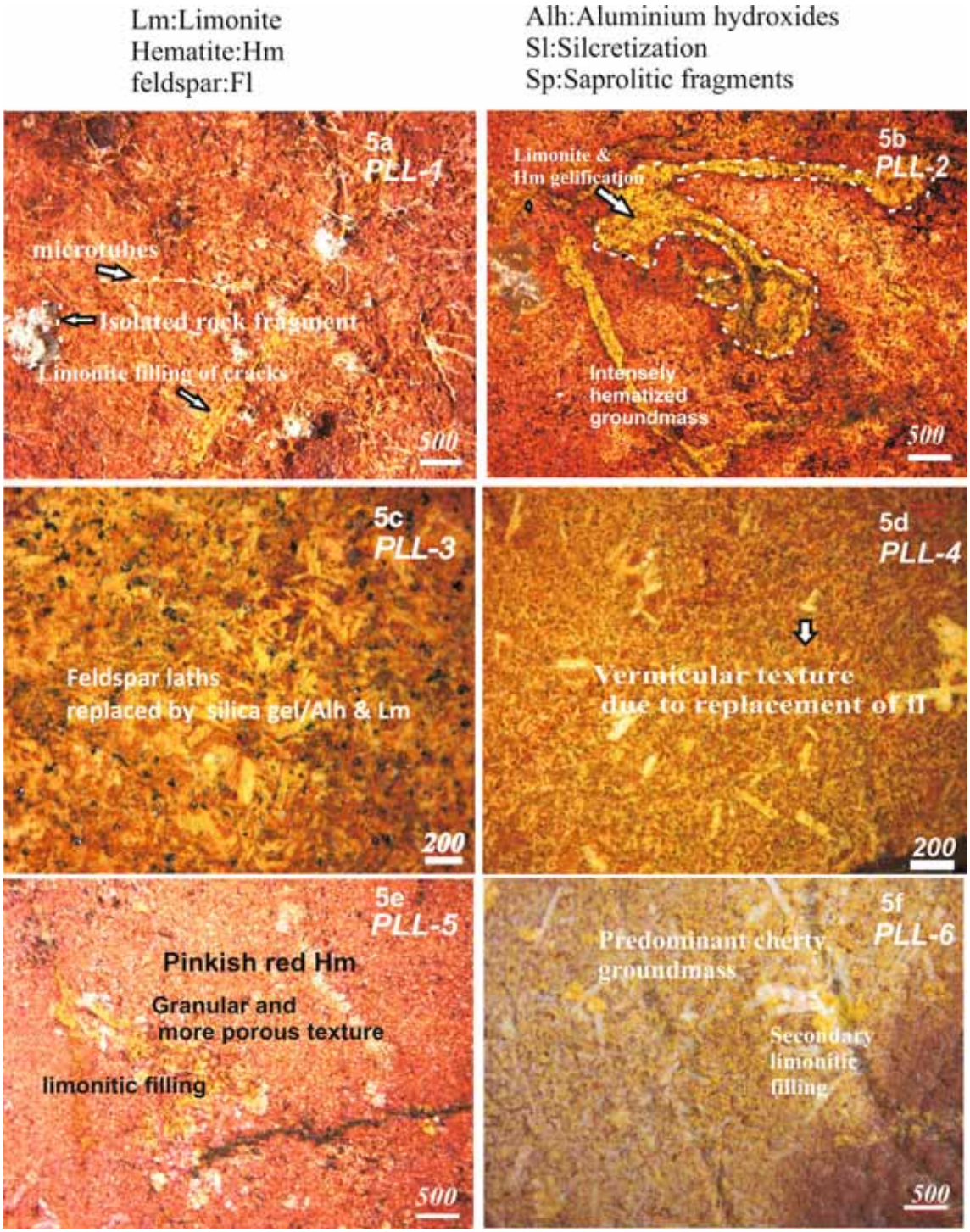

Figure 5. (**a–w**) Ore microphotographs representing each sampled horizon from bottom towards top. Details are described in text.

mixed brownish banding (figure 5o). This suggested an incipient development of liesegang rings/bands as a result of colloidal gel precipitation that is more distinct in the later units (figure 5p and q). PLL-16 shows contrasting purple to maroon (bluish grey to brown) intermixed groundmass without any nodular development. It shows cavity filling with white kaolinitic and silcrete material. The irregular geometry of the pores and the corroded hematite boundaries on the weathered rock fragments suggest intense solution–precipitation activity (figure 5p). Megascopically, this horizon shows contrasting bluish grey to brown intermixed horizons without any nodular development but

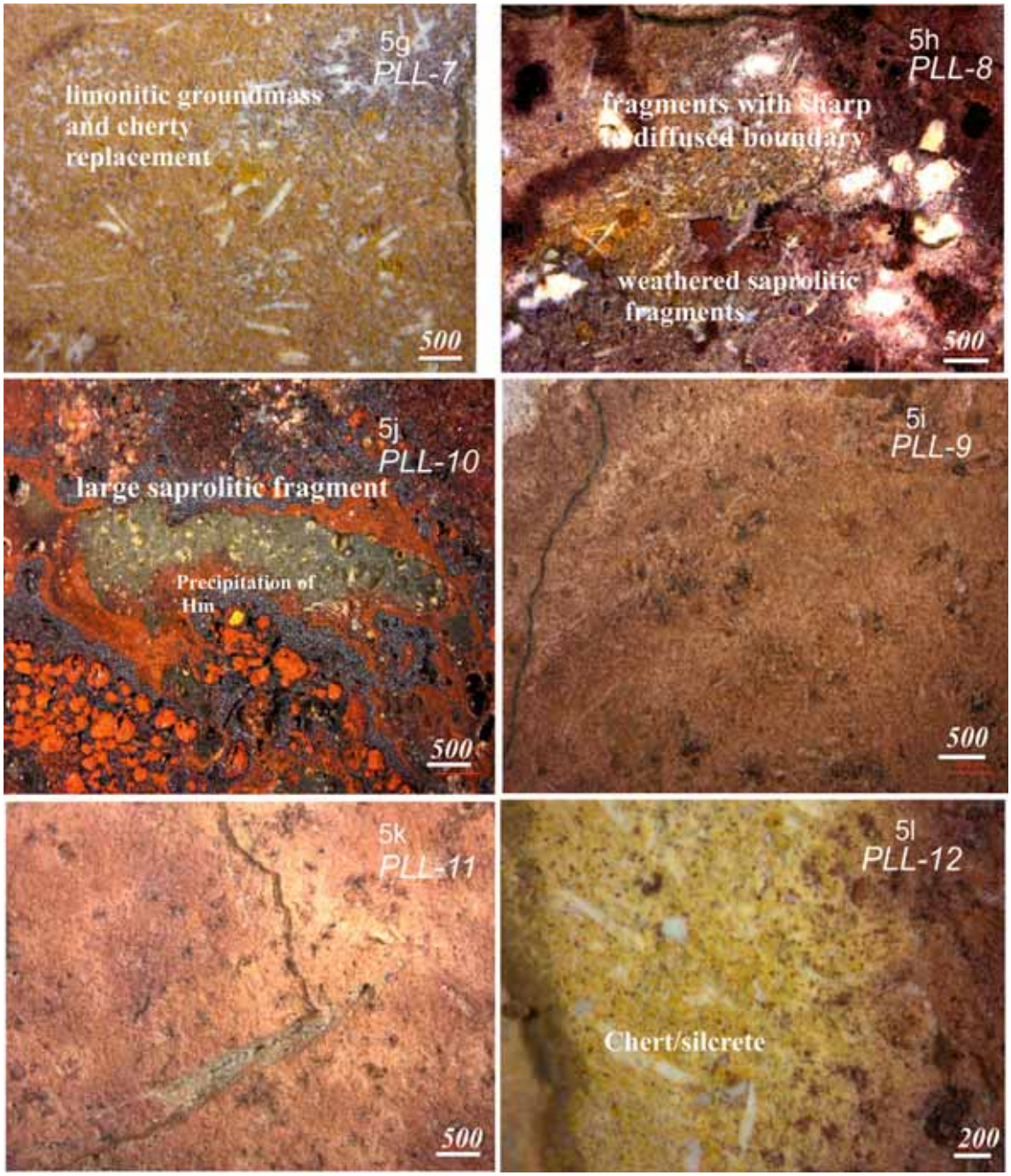

Figure 5. (*Continued.*)

cavity filling by clay (kaolinite). The sample PLL-17 under microscope shows bluish grey to maroon groundmass filled with siliceous solution (silcertized). The groundmass shows eroded plagioclase laths replaced by siliceous mass. It shows intense solution activity with colloidal filling of the pores (figure 5q). The sample PLL-18 under microscope shows distinct bright cherry red (/brick red) hematitic groundmass with saprolitic fragments and minor secondary-limonitic filling (figure 5r). Megascopically, the specimen showed significant change by abundance of reddish brown and yellowish brown mottles and greyish white filling in irregular porous veins (see figure 4). In this horizon, the porosity is increased compared to PLL-17. The sample PLL-19 shows contrasting lighter as well as brighter reddish brown and yellowish brown mottles and grayish white filling in irregular porous veins. The boundaries are sharp, irregular and distinct and the porosity is increased relative to the previous horizons. It shows deeply weathered basalt (saprolitic) with higher porosity, pinkish

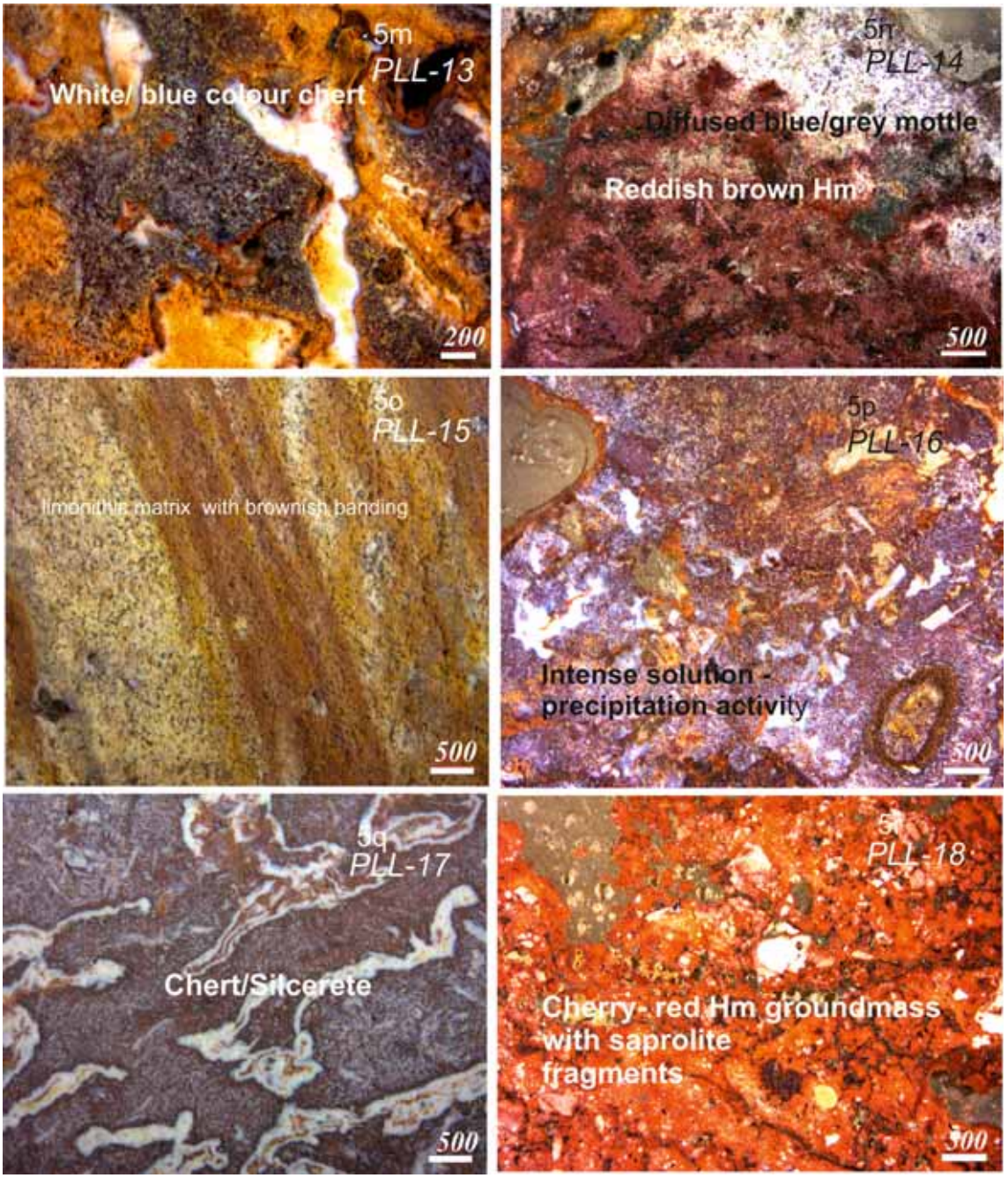

Figure 5. (*Continued.*)

hematite, limonite and kalolinitic masses (figure 5s). The occurrence of weathered basalt (/saprolite) at this higher horizon depict allochthonous input that was again subjected to re-lateritization. PLL-20 shows rounded (tube like?) masses of hematite surrounded by deeply weathered saprolites. Traces of yellow limonitic filling are also observed, whereas elongated lenticular fractures (open spaces) of 1–2 mm are filled with hematitic solution (figure 5t). In hand sample, it shows diffused reddish brown to pink colour masses with cavity filling by greyish white to dark grey clayey material. PLL-21 is a complex horizon with less weathered, massive, low porosity groundmass and saprolite fragments being altered and filled with limonites (figure 5u). The introduction of rock fragments (/saprolitic) at this higher level further is indicative of allochthonous input. PLL-22 shows dull yellow massive limonitic groundmass replacing the saprolitic ground mass (figure 5v). Megascopically, this horizon showed encrusted (duricrust like) units of dull brownish grey, yellow (limonite),

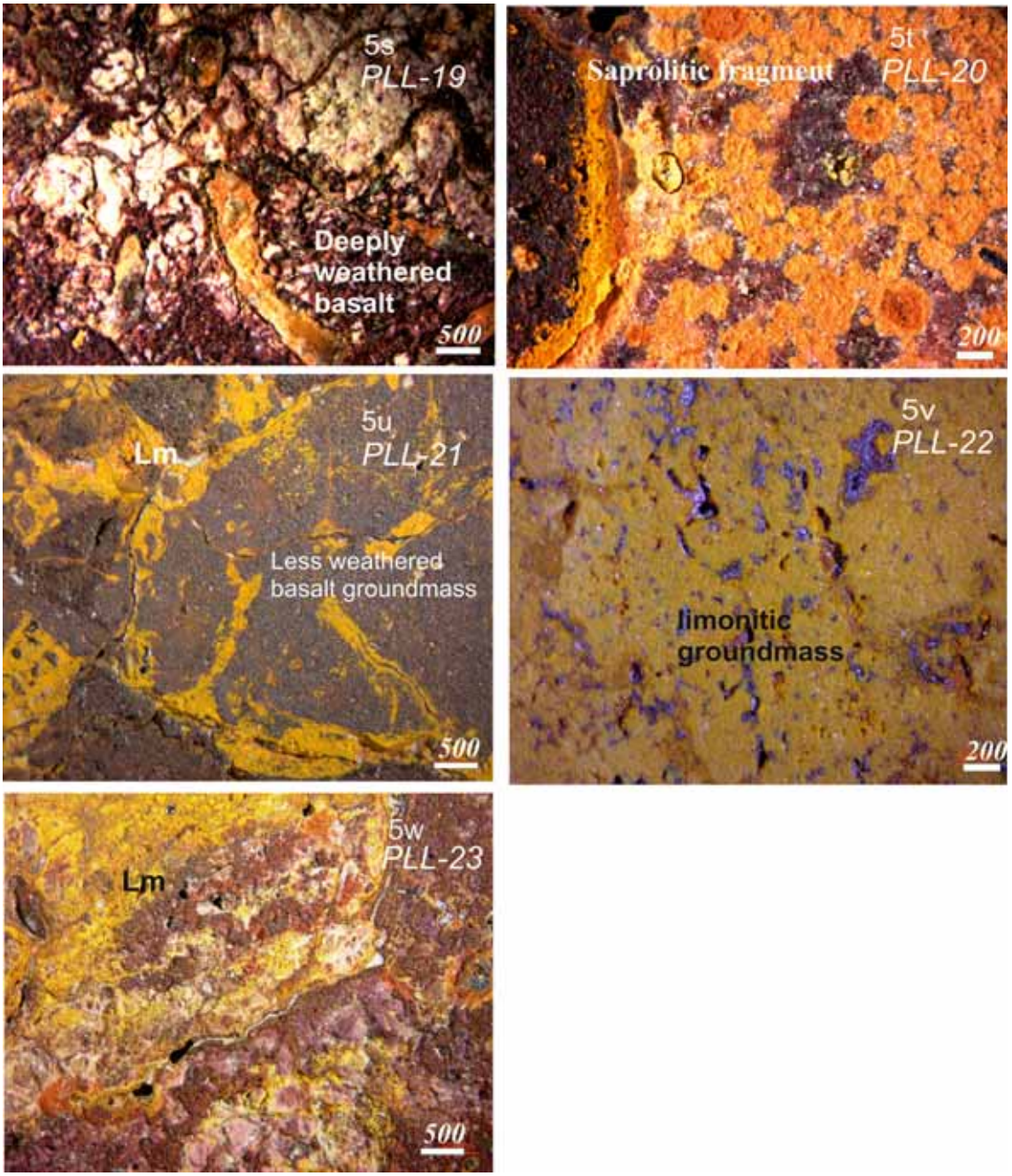

Figure 5. (*Continued.*)

pinkish red (hematite matrix) and metallic black Fe–Mn oxides with sharp and irregular boundaries. PLL-23 is a massive complex encrusted (duricrust) unit showing dull brownish grey (goethite?), bright yellow (limonite), pinkish red (hematitic matrix) and the metallic black Fe–Mn oxides having sharp and irregular boundaries (figure 5w). It shows pink ferric iron oxide along with limonite. Megascopically (figure 4), this horizon shows incipient limonitic and pisolitic growth with irregular boundaries.

The XRD analysis of representative bulk samples shows kaolinite peaks at 7.18, 3.571 2.438 A°, hematite peaks at 2.69, 1.67 A°, gibbsite at 4.850 A° and goethite at 4.15 A° (see figure 7). Further the clay separation of a representative sample from bulk (PLL-19) confirms the occurrence of these peaks in bulk samples that match with the peaks of kaoinite, gibbsite, hematite and goethite. The gibbsite occur with high concentration in the uppermost horizons (PLL 21–23, see table 1 and figure 7). Whereas, other minerals are distributed in the lower horizons. The lowermost

Table 2. *Summary of magnetic data of Patan laterite profile samples.*

Sample name	χ_{lf}	χ_{fd}%	χ_{fd}	BCR	χ_{ARM}	SIRM	S-ratio	Soft-IRM	HIRM
PLL-23	2.04	8.47	0.17	666	11.21	909.78	0.77	23.73	804.30
PLL-22	1.74	12.50	0.22	424	6.33	1750.93	0.51	44.56	1326.25
PLL-21	4.47	7.09	0.32	412	51.85	9141.57	0.42	163.57	6498.15
PLL-20	2.05	13.73	0.28	410	29.50	2983.32	0.32	75.25	1962.16
PLL-19	4	7.59	0.30	462	27.34	9266.72	0.58	118.84	7316.79
PLL-18	2.64	13.56	0.36	490	53.76	3745.42	0.51	88.73	2834.53
PLL-17	1.09	8.33	0.09	590	14.92	1604.62	0.69	53.24	1357.86
PLL-16	1.15	18.52	0.21	504	3.45	2498.99	0.63	39.65	2030.76
PLL-15	1.16	0	0	554	5.90	642.48	0.59	23.15	510.86
PLL-14	0.82	0	0	536	5.70	1593.88	0.72	32.94	1371.58
PLL-13	1.74	2.94	0.05	466	8.48	1427.27	0.47	103.91	1046.57
PLL-12	1.14	10.00	0.11	472	2.25	1500.11	0.48	72.90	1110.44
PLL-11	1	21.05	0.21	430	1.25	1235.97	0.41	76.39	870.40
PLL-10	0.89	33.33	0.30	574	1.43	1504.31	0.71	48.54	1288.00
PLL-9	1.30	0	0	480	1.72	1198.48	0.56	51.60	935.04
PLL-8	1.75	6.06	0.11	538	2.99	587.05	0.56	37.27	459.02
PLL-7	5.64	0	0	15	720.16	1813.97	−0.71	1294.44	264.48
PLL-6	7.53	6.80	0.51	16	831.21	1943.09	−0.65	1187.19	339.00
PLL-5	40.33	0.87	0.35	2	2117.28	3361.37	−0.88	3101.31	200.29
PLL-4	97.88	0.57	0.56	2	3571.53	9431.54	−0.91	8218.09	404.57
PLL-3	84.54	0	0	12	6203.94	17884.11	−0.92	14281.51	709.37
PLL-2	45.20	0	0	16	5225.46	18258.23	−0.92	11492.18	750.00
PLL-1	46.84	1.28	0.60	15	5337.07	20048.21	−0.94	12771.13	580.53
PLL-0	25.79	0.90	0.23	27	3611.16	22560.60	−0.95	9026.63	583.35

The units of χ_{lf} and $\chi_{fd} = 10^{-8}$ m^3 545 kg^{-1}, BCR = mT, $\chi_{ARM} = 10^{-8}$ m^3 kg^{-1} and for SIRM, Soft-IRM and HIRM = 10^{-5}A m^2 kg^{-1}. The units are also applicable to figure 6.

horizons (PLL-2) (see table 1) are dominated by kaolinite. Hematite and limonite observed in the ore microscopy are not detected in XRD, confirming amorphous nature of majority of the samples in lower and middle horizons.

Overall the ore microscopic observations indicated interplay of hematite and limonite as solution activity. The occurrence of pure clay is minor and the clay might have accompanied with limonite and hematite masking its original colour. Saprolite and weathered rock fragments are encountered at various levels depicting detrital influxes. This suggests contemporary lateral surficial inputs likely to be during heavy precipitation.

5. Magnetic results

The mineral magnetic data for PLL profile is accounted in table 2. This profile has been subdivided into four broad zones based on distinct variations in the mineral magnetic parameters, ore microscopy and field characters (tables 1–2 and figure 5); and is described below.

5.1 *Deccan basalt protolith (PLL-0)*

The lowermost zone marked by unweathered basalt (PLL-0) show high χ_{lf} of the order $\sim 25.79 \times 10^{-8}$ m^3 kg^{-1} depicting high ferrimagnetic concentration (table 2). The χ_{fd}% of ∼0.90 and χ_{fd} $\sim 0.23 \times 10^{-8}$ m^3 kg^{-1} indicate absence of superparamagnetic (SP) ferrimagnetic particles in the parent material (table 2). Very high SIRM value indicates high ferromagnetic concentration in the protolith. Soft-IRM and χ_{ARM} show abundance of pseudo single domain (PSD) to single domain (SD) ferriagnetic grains. The S-ratio (−0.95) and $B_{(0)CR}$ (27 mT) further indicate the dominant ferrimagnetic composition.

5.2 *Saprolite–Ferrecrete transition Zone I (PLL-1 to 3)*

This zone is marked by change in textural appearance and colour properties relative to protolith. Minor diffused limonitic mottling and nodular development could be seen. The χ_{lf} for this

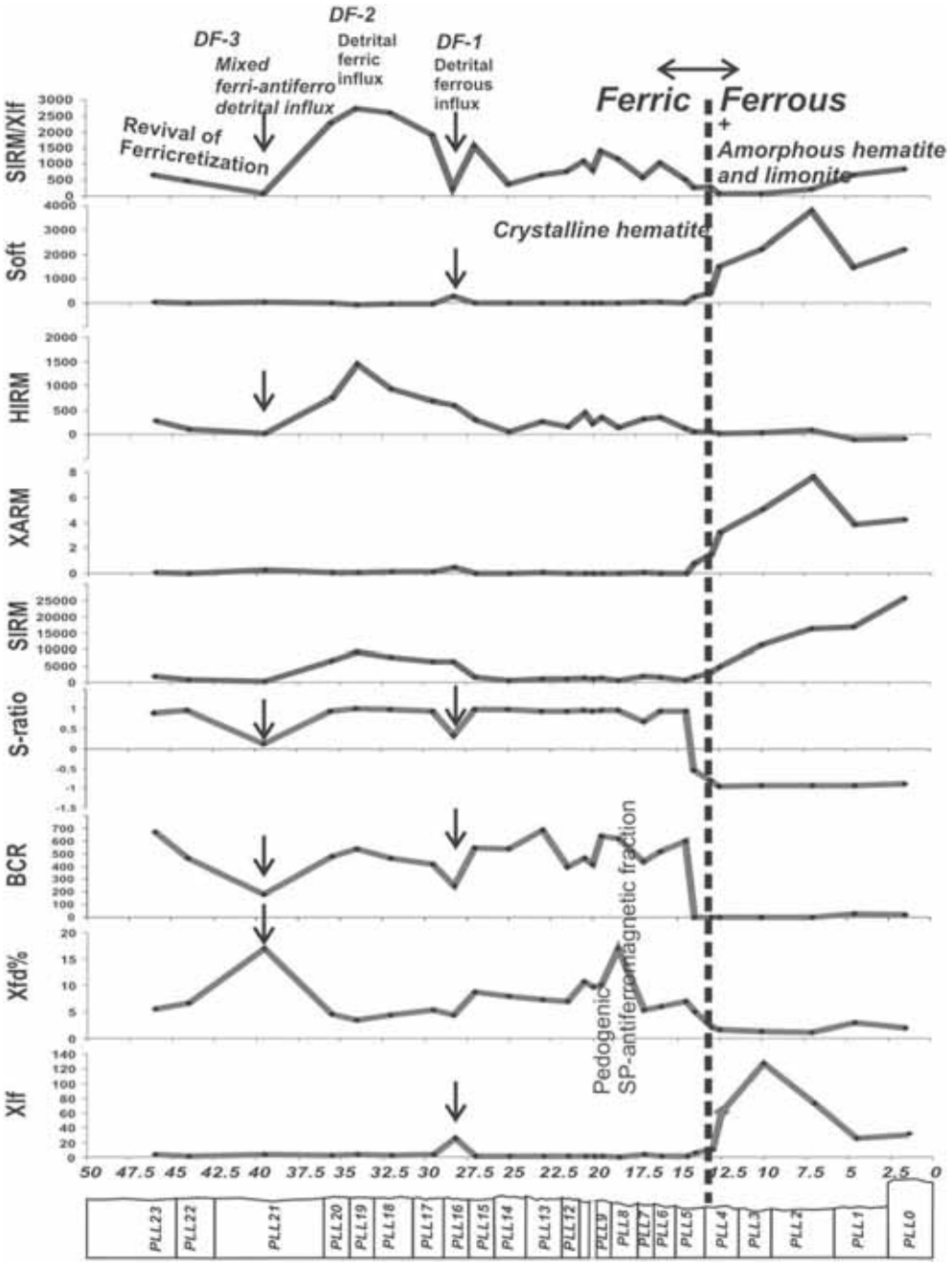

Figure 6. Mineral magnetic parameters plotted against the studied profile of PLL section. Major boundary and events are marked and described in the text.

zone ranges from ∼45 to 84 ($\times 10^{-8}$ m^3 kg^{-1}) suggesting higher ferrimagnetic concentration relative to the parent basalt. This is likely due to dissolution of majority of paramagnetic and diamagnetic constituent minerals due to weathering and solution activity. The χ_{lf} shows increasing trend from PLL-1 to PLL-3. The χ_{fd}% and χ_{fd} show maximum value of ∼1.28% and 0.60 × 10^{-8} m^3 kg^1, respectively (table 2) indicating absence of SP ferrimagnetic mineral phases. In contrast to χ_{lf}, the SIRM shows decreasing concentration of coarser multi-domain (MD) to (PSD) particles as a result of dissolution during chemical weathering. The Soft-IRM and χ_{ARM} co-vary with χ_{lf} and show an increasing trend indicating higher concentration of SD particles. The S-ratio (−0.88 to −0.92) and $B_{(0)CR}$ (12–16 mT) clearly indicate dominant ferrimagnetic mineralogy marked by MD ferrimagnets. The HIRM does not show any significant change in this zone.

5.3 *Saprolite–Ferrecrete transition Zone II (PLL-4 to 7)*

The χ_{lf}, SIRM, Soft-IRM and χ_{ARM} show decreasing trends indicating depleted ferrimagnetic concentration. The $\chi_{fd}\%$ and χ_{fd} values further show absence of SP ferrimagnetic particles. The $B_{(0)CR}$ varying from 2 to 16 mT in this horizon indicate ferrimagnetic mineralogy with predominance of MD grains. The S-ratio (−0.91 to −0.71) depict relative dominance of ferrimagnetic minerals (table 2). However, higher positive S-ratios relative to the protolith and incipient saprolitic zones suggest increased concentration of anti-ferromagnetic minerals. However, the hematite is likely to be of amorphous origin and hence the HIRM did not show any significant change. This horizon therefore indicates a complex of ferrimagnetic and anti-ferromagnetic mineralogy, and mineral magnetic properties are dominated by ferrimagnetism due to their higher sensitivity to the applied magnetic fields.

5.4 *Ferricrete horizons (PLL-8 to 23)*

This zone is marked by a significant drop in χ_{lf}, SIRM, Soft-IRM and χ_{ARM} depicting lowest ferrimagnetic concentration within the profile. In this zone, several samples and specifically the topmost samples show significant $\chi_{fd}\%$ from 7 to 18.5%. Few abnormally high $\chi_{fd}\%$ values in PLL-11 and PLL-10 are also recorded, although the χ_{fd} showed a maximum value of $\sim 0.36 \times 10^{-8}$ m^3 kg^{-1} similar to low concentration of SP ferrimagnetic grains (table 2). However, as the mineralogy is dominantly anti-ferromagnetic, the SP fraction appears to be of anti-ferromagnetic nature rather than ferromagnetic SP. The $B_{(0)CR}$ and S-ratio sharply demarcate saprolite–ferricete boundary. $B_{(0)CR}$ ranges from ∼228 to 666 mT indicating dominant anti-ferromagnetic mineralogy (hematite and goethite). The S-ratio shows positive value in this zone ranging from 0.32 to 0.77 further depict overall dominance of anti-ferromagnetic minerals. The HIRM shows gradual increasing trend towards top of the profile. Amongst all the parameters, χ_{lf} being most portable to be measured, shows a greater scope for regional mapping of the saprolite–ferricrete boundary in the field. The profile in the lower part (∼0 to 13 m) shows enrichment of χ_{lf}, χ_{ARM} and $Soft_{IRM}$ with gradual decrease in SIRM without any alternation to S-ratio and $B_{(0)CR}$. This part in field and ore microscopy is observed for transition from weathered basalt to saprolite. The increase in χ_{lf} along with χ_{ARM} and $Soft_{IRM}$ is probably due to enrichment of SD ferrimagnets. The SD ferrimagnets in the present case can be formed by reduction of domain size of ferrimagnets by dissolution during chemical weathering or it can be simply anti-ferromagnetic SD grains. Under microscope we observed good amount of hematite and limonite in this lower interval (i.e., 0–13 m), which is not traceable by any of the rock magnetic parameters suggesting its amorphous nature within the highly ferrimagnetic background. After this there is a sharp boundary demarcating the ferrous to ferric transition in the profile marked in figure 6. The amorphous hematite (and limonite) below this boundary appears to have been rapidly precipitated in the pore spaces made available during/after formation of saprolites. Above this horizon, the crystalline hematites are formed slowly during the ferricretization and is also associated with amorphous limonite and hematite. The crystalline and amorphous hematites are likely to have paragenetic association with the later introduced by secondary processes. Upwards in the profile, the anti-ferromagnetism is very well maintained with possible appearances of goethite that is marked by very high coercivity values (Sangode and Bloemendal 2004). In this upper part of the profile (>13 m) there are episodes of detrital ferrous and ferric inputs marked in figure 6 and also observed under the microscopy. Such detrital episodes appear to have temporarily arrested the ongoing lateritization process and later the ferricretization was revived again. These detrital episodes can therefore be inferred as lateral influxes during heavy precipitation. The lateral influxes brought the materials of saprolitic as well as lateritic catchment. The cavity fillings by hematite and limonite as secondary minerals also support such activity. More number of sections on this lateritic plateau need be studied to examine or endorse the above inferences. We further suggest a detailed mineral magnetic mapping of the Deccan high level lateritic profiles in the Western Ghat escarpment to delineate the paleosurfaces and their evolution, such as magnetic susceptibility mapping of the sharp ferri/anti-ferromagnetic boundary as observed here.

Overall the mineral magnetism showed a sharp ferri- to anti-ferromagnetic boundary falling at ∼13 m level (during PLL-4 and 5). The hematites suggest at least two varieties (amorphous and crystalline). The $\chi_{fd}\%$ showed significant increase

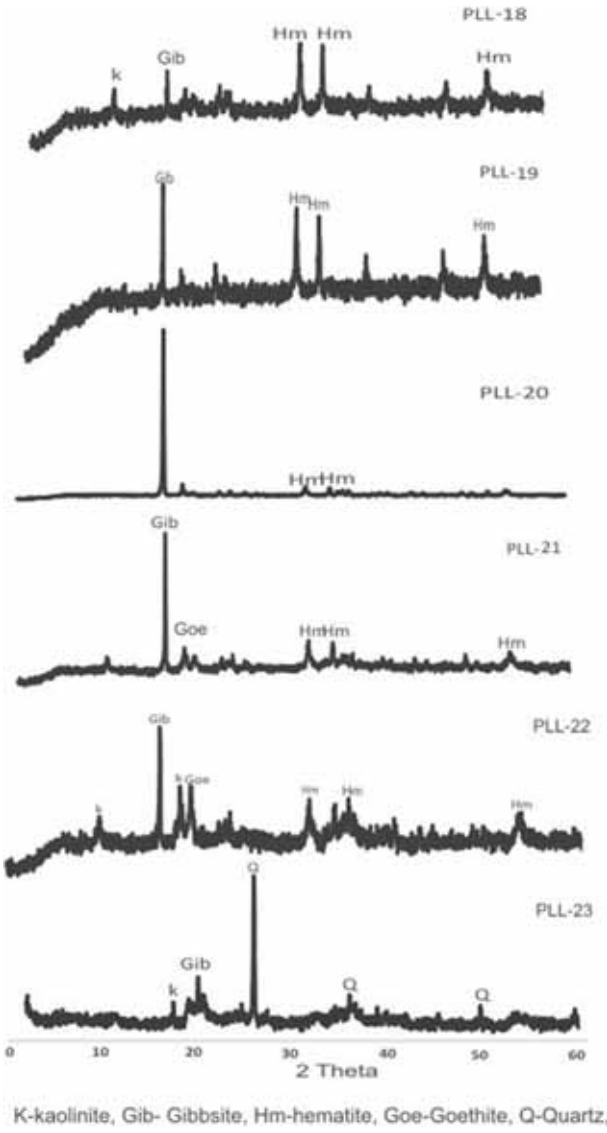

Figure 7. XRD spectra of representative samples from the PLL section described in text.

within the anti-ferromagnetic phase of the profile depicting its control by the anti-ferromagnetic SP fraction likely to be of amorphous nature (limonite and hematite). Whereas the other rock magnetic parameters (e.g., HIRM and $B_{(0)CR}$) are more sensitive to the crystalline varieties of hematite/goethite. The detrital influx also appears to be of mixed ferri- and anti-ferromagnetic nature, as the catchment itself was saprolitic and ferricretized during the higher levels of lateritization. The penultimate stage represents arresting of the geochemical reactions in the composite growth due to loss in porosity. However, development of secondary porosity due to desiccation- or stabilization-cracks resulted into precipitation of limonites into deeper levels. The frequent lateral surficial input appears to have added to the thickness of the lateritic profiles in this region. Whereas, these episodes must have arrested the ongoing geochemical front of latertization; disengaging the maturity towards bauxitization.

This work attempted to develop an understanding on the allochthonous inputs during the process of lateritization. The sporadic detrital (allogenic) influxes during the development of the lateritic profile are marked (figures 6 and 8). The influx resulted into break in the process which again reclaimed. The authigenic matter contained lithic fragments, saprolitic fragments as well as ferricrete fragments as seen under microscope and marked by ferrimagnetic peaks in these horizons. The re-lateritization produced diffused gradation (no sharp boundary for the break to be seen in the field). The entire profile is developed episodically arresting and reclaiming the process of lateritization. This further explains the large thickness of profile despite of any significant maturity to be observed in classical lateritic profiles. The immaturity can be deciphered by the overall absence of typical lower horizons such as 'associated-pallid-mottled zones' or the development of bauxites. The total thickness of >20 m in the present case which is greater than classical laterite profiles is thus explained. In the present work we relate the SP fraction to anti-ferromagnetic-pigmentary/amorphous fractions rather than the SP ferrimagnets. We postulate this in the instance the rock magnetic properties do not detect hematite although it is visible in ore microscope (and hand specimen). This suggested that the hematite/limonite are of amorphous type, which is also not traceable through XRD analysis.

6. Conclusion

Integrated studies based on field megascopic observations, ore microscopy, mineral magnetism and XRD spectroscopy from a well exposed lateritic profile are made to represent some of the characteristic processes of lateritization in the Deccan upland lateritic sequence. This study records (i) a sharp ferri- to anti-ferromagnetic boundary equivalent of saprolite/ferricrete transition depicting a total of ∼32 m thick ferricrete profile above, (ii) episodic lateral influx at various levels within the profile, (iii) low amount of clays (kaolinites) distributed throughout the profile, (iv) occurrence of gibbsite in the later phase/upper horizons. The studies delineate amorphous

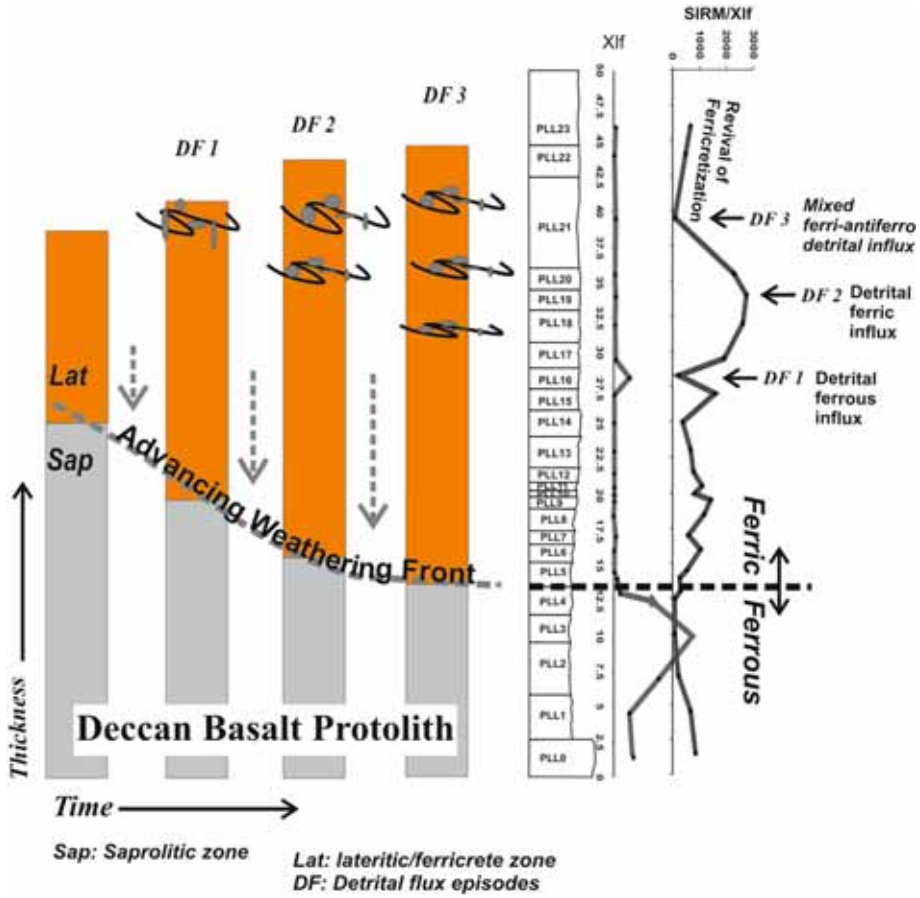

Figure 8. Possible model explaining episodic evolution of the studied lateritic profile with advancing weathering front (/time).

and crystalline varieties of anti-ferromagnetic iron oxide minerals (e.g., limonite, hematite, goethite) and their paragenetic interplay throughout the profile. Introduction of secondary oxides are controlled by changes in porosity. The considerably thick nature of the Deccan lateritic profiles without attainment of maturity with above characteristics therefore indicate a composite growth by autochthonous and allochthonous processes.

Acknowledgements

We acknowledge Head, Department of Geology, Savitribai Phule Pune University for the Departmental Research Grant to conduct the fieldwork and the DST-FIST (grant SR/FST/ESII-101/2010) for laboratory support and DST-PURSE program for fellowship to JS. Dr Priyeshu Srivastava is acknowledged for suggestions and help during analysis and interpretations. Finally, two anonymous reviewers are acknowledged for critical examination and suggestions that improved the manuscript to a great extent.

References

Achyuthan H 1996 Geomorphic evolution and genesis of laterites from the east coast of Madras, Tamil Nadu; *Geomorphology* **16** 71–76.

Amouric M, Baronnet A, Nahon D and Didier P 1986 Electron microscopic investigations of iron oxyhydroxides and accompanying phases in lateritic iron-crust pisolites; *Clay Clay Miner.* **34** 45–52.

Anand R R and Gilkes R J 1987 Iron oxides in lateritic soils from Western Australia; *J. Soil Sci.* **38** 607–622.

Babechuk M G, Widdowson M and Kamber B S 2014 Quantifying chemical weathering intensity and trace element release from two contrasting basalt profiles, Deccan Traps, India; *Chem. Geol.* **363** 56–75.

Babechuk M G, Widdowson M, Murphy M and Kamber B S 2015 A combined Y/Ho, high field strength element (HFSE) and Nd isotope perspective on basalt weathering, Deccan Traps, India; *Chem. Geol.* **396** 25–41.

Balsam W, Ji J and Chen J 2004 Climatic interpretation of the Luochuan and Lingtai loess sections, China, based on changing iron oxide mineralogy and magnetic susceptibility; *Earth Planet. Sci. Lett.* **223** 335–348.

Beauvais A and Colin F 1993 Formation and transformation processes of iron duricrust systems in tropical humid environment; *Chem. Geol.* **106** 77–101.

Bonnet N J, Beauvais A, Arnaud N, Chardon D and Jayananda M 2014 First $^{40}Ar/^{39}Ar$ dating of intense late

Palaeogene lateritic weathering in peninsular India; *Earth Planet. Sci. Lett.* **386** 126–137.

Bonnet N J, Beauvais A, Arnaud N, Chardon D and Jayananda M 2016 Cenozoic lateritic weathering and erosion history of peninsular India from $^{40}Ar/^{39}Ar$ dating of supergene K–Mn oxides; *Chem. Geol.*, http://dx.doi.org/10.1016/j.chemgeo.2016.04.018.

Borger H and Widdowson M 2001 Indian laterites, and lateritious residues of southern Germany: A petrographic, mineralogical, and geochemical comparison; *Zeitschrift fur Geomorphologie* **45(2)** 177–200.

Buggle B, Hambach U, Müller K, Zöller L, Marković S B and Glaser B 2014 Iron mineralogical proxies and Quaternary climate change in SE-European loess–paleosol sequences; *Catena* **117** 4–22.

Cornell R M and Schwertmann U 2003 *The iron oxides: Structure, properties, reactions, occurrences and uses*; John Wiley & Sons.

Heller F and Evans M E 1995 Loess magnetism.; *Rev. Geophys.* **33(2)** 211–240.

Jordanova D and Petersen N 1999 Palaeoclimatic record from a loess–soil profile in northeastern Bulgaria – I. Rock magnetic properties; *Geophys. J. Int.* **138** 520–532.

Kumar A 1986 Palaeolatitudes and the age of Indian laterites; *Palaeogeogr. Palaeoclimatol. Palaeoecol.* **53** 231–237.

Liu Q, Bloemendal J, Torrent J and Deng C 2006 Contrasting behavior of hematite and goethite within paleosol S5 of the Luochuan profile, Chinese Loess Plateau; *Geophys. Res. Lett.* **33** L20301, https://doi.org/10.1029/2006gl027172.

Long X, Ji J and Balsam W 2011 Rainfall-dependent transformations of iron oxides in a tropical saprolite transect of Hainan Island, South China: Spectral and magnetic measurements; *J. Geophys. Res.-Earth* **116(F3).**

Long X, Ji J, Balsam W, Barrón V and Torrent J 2015 Grain growth and transformation of pedogenic magnetic particles in red Ferralsols; *Geophys. Res. Lett.* **42** 5762–5770, https://doi.org/10.1002/2015gl064678.

Meshram R R and Randive K R 2011 Geochemical study of laterites of the Jamnagar district, Gujarat, India: Implications on parent rock, mineralogy and tectonics; *J. Asian Earth Sci.* **42** 1271–1287.

Mishra S, Deo S and Rajaguru S N 2007 Some observations on laterites developed on Deccan Trap: Implications for post-Deccan Trap denudational history; *J. Geol. Soc. India* **70** 521–525.

Ollier C D and Rajaguru S N 1989 Laterite of Kerala (India); *Geogr. Fis. Din. Quat.* **12** 2–33.

Ollier C D and Sheth H C 2008 The High Deccan duricrusts of India and their significance for the 'laterite' issue; *J. Earth Syst. Sci.* **117** 537–551.

Patel P K 1987 Lateritization and bentonitization of basalt in Kutch, Gujarat State, India; *Sedim. Geol.* **53** 327–346.

Sahasrabudhe Y S and Rajaguru S N 1990 The laterites of the Maharashtra State; *Bull. Decc. Coll. Res. Inst.* **49** 357–370.

Sangode S J and Bloemendal J 2004 Pedogenic transformation of magnetic minerals in Pliocene–Pleistocene palaeosols of the Siwalik Group, NW Himalaya, India; *Palaeogeogr. Palaeoclimatol. Palaeoecol.* **212** 95–118.

Schellmann W 1994 Geochemical differentiation in laterite and bauxite formation; *Catena* **21** 131–143.

Schmidt P W, Prasad V and Ramam P K 1983 Magnetic ages of some Indian laterites; *Palaeogeogr. Palaeoclimatol. Palaeoecol.* **44** 185–202.

Schwertmann U 1958 The effect of pedogenic environments on iron oxide minerals; In: *Advances in soil science* (ed.) Stewart B A, Springer, New York, NY, Vol. 1, pp. 171–200.

Schwertmann U 1988 Occurrence and formation of iron oxides in various pedoenvironments; In: *Iron in soils and Clay Miner.*, Springer, Dordrecht, pp. 267–308.

Schwertmann U 1993 Relations between iron oxides, soil colour, and soil formation; *SSSA Spec. Publ.* **31** 51–69.

Schwertmann U and Cornell R M 2000 *Iron oxides in the laboratory* (Vol. 2). Weinheim: Wiley-Vch.

Srivastava P, Sangode S J and Torrent J 2015 Mineral magnetic and diffuse reflectance spectroscopy characteristics of the Deccan volcanic bole beds: Implications to genesis and transformations of iron oxides; *Geoderma* **239** 317–330.

Thompson R and Oldfield F 1986 *Environmental magnetism*; Allen and Unwin Press, London, 227p.

Torrent J, Schwertmann U and Schulze D G 1980 Iron oxide mineralogy of some soils of two river terrace sequences in Spain; *Geoderma* **23(3)** 191–208.

Torrent J, Barrón V and Liu Q 2006 Magnetic enhancement is linked to and precedes hematite formation in aerobic soil; *Geophys. Res. Lett.* **33** L02401, https://doi.org/10.1029/2005gl024818.

Turner Gillian M 1997 Environmental magnetism and magnetic correlation of high resolution lake sediment records from Northern Hawke's Bay, New Zealand; *New Zeal. J. Geol. Geop.* **40(3)** 287–298.

Widdowson M 1997 Tertiary palaeosurfaces of the SW Deccan, Western India: Implications for passive margin uplift; *Geol. Soc. London* **120(1)** 221–248.

Widdowson M 2007 Laterite and ferricrete; In: *Geochemical Sediments and Landscapes* (eds) Nash David J and McLaren Sue J, Oxford, UK: Wiley-Blackwell, pp. 46–94.

Widdowson M and Gunnell Y 1999 Tertiary palaeosurfaces and lateritization of the coastal lowlands of western peninsula India; *Palaeowea, Palaeosurf and Rel Cont Deposits, Int As Sed.*

Widdowson M and Cox K G 1996 Uplift and erosional history of the Deccan Traps, India: Evidence from laterites and drainage patterns of the Western Ghats and Konkan Coast; *Earth Planet. Sci. Lett.* **137** 57–69.

Widdowsow M and Gunnell Y 2009 Lateritization, geomorphology and geodynamics of a passive continental margin: The Konltan and Kanara coastal lowlands of western peninsular India; *Palaeowea, Palaeosurf and Rel Cont Deposits* **73** 245.

Wimpenny J, Gannoun A, Burton K W, Widdowson M, James R H and Gislason S R 2007 Rhenium and osmium isotope and elemental behaviour accompanying laterite formation in the Deccan region of India; *Earth Planet. Sci. Lett.* **261** 239–258.

Zeese R, Schwertmann U, Tietz G F and Jux U 1994 Mineralogy and stratigraphy of three deep lateritic profiles of the Jos Plateau (Central Nigeria); *Catena* **21** 195–214.

Corresponding editor: Santanu Banerjee